

Cite this: *J. Mater. Chem. A*, 2021, **9**, 16982

Multi-scale investigation of heterogeneous swift heavy ion tracks in stannate pyrochlore[†]

Eric C. O'Quinn,^a Cameron L. Tracy,^b William F. Cureton,^a Ritesh Sachan,^c Joerg C. Neufeind,^d Christina Trautmann^{ef} and Maik K. Lang^{*a}

$\text{Er}_2\text{Sn}_2\text{O}_7$ pyrochlore was irradiated with swift heavy Au ions (2.2 GeV), and the induced structural modifications were systematically examined using complementary characterization techniques including transmission electron microscopy (TEM), X-ray diffraction (XRD), and neutron total scattering with pair distribution function (PDF) analysis. Each technique probes different aspects and length scales of the transformed material regions. TEM revealed a core–shell ion track structure—an amorphous core surrounded by a disordered, anion-deficient fluorite shell—which was confirmed by XRD. Neutron total scattering, with sensitivity to the oxygen sublattice, provided relative fractions of amorphous and disordered fluorite phases and confirmed the presence of a defective pyrochlore phase, which largely maintains its structural ordering but is clearly distinct from the pristine pyrochlore matrix. This defect-rich pyrochlore phase forms a halo extending radially beyond the well-characterized core–shell track morphology observed in electron micrographs. Despite their differing long-range periodicity, the short-range structures of the amorphous, disordered, and defective pyrochlore phases are all modeled well with a weberite-type configuration. Evolution of the phase fractions with increasing ion fluence was examined to ascertain the phase-to-phase pathways that occur during primary and secondary ion impact. This approach extends knowledge about the multi-scale response of stannate pyrochlores to swift heavy ion irradiation in the electronic energy loss regime and improves existing track-overlap models.

Received 10th June 2021
 Accepted 19th July 2021

DOI: 10.1039/d1ta04924k
rsc.li/materials-a

1. Introduction

Complex oxide materials that adopt the pyrochlore structure ($\text{A}_2\text{B}_2\text{O}_7$ stoichiometry, $9 \text{ \AA} < a_0 < 12 \text{ \AA}$) exhibit a wide variety of exotic properties: for example, giant magnetoresistance,¹ geometric frustration² and spin ice states,³ oxygen ion conductivity,⁴ superconductivity,⁵ and exceptional radiation stability.⁶ This diversity results from the structure's compositional accommodation of over 500 combinations of A- and B- site cations.⁷ Belonging to isometric space group $Fd\bar{3}m$, the pyrochlore structure (Fig. 1a) can be imagined as a $2 \times 2 \times 2$ superstructure of AO_2 fluorite subunits, containing two distinct cation sites ($16c$, $16d$), two distinct anion sites ($48f$, $8b$), and an

ordered anion vacancy ($8a$). The A-site cation is eight-coordinated and resides in a distorted cubic coordination polyhedron, while the B-site cation is six-coordinated and occupies a distorted octahedron. Though the large unit cell ($V_0 > 10^3 \text{ \AA}^3$) contains 88 atoms, the crystallography of any pyrochlore phase can be constrained fully by two structural degrees of freedom:⁷ the unit cell parameter (a_0) and the position of the oxygen ion at Wyckoff equiopoint $48f(x)$.

The structural stability of these compounds is strongly linked to the ratio of the cationic radii, r_A/r_B , with the pyrochlore structure preferred when $1.46 \leq r_A/r_B \leq 1.78$.⁷ Above a ratio of 1.78, a monoclinic, perovskite-type structure is preferred; below 1.46, a cation-disordered, anion-deficient fluorite phase is the most stable configuration. In compounds for which the ordered pyrochlore structure is stable, extreme conditions (e.g., pressure, temperature, and irradiation) may drive an order–disorder transition to the disordered, anion-deficient fluorite structure (Fig. 1b).⁸ This process is commonly depicted as random mixing of A and B type cations on the cation sublattice, random mixing of anions and vacant sites on the anion sublattice, and a corresponding reduction in the periodicity of the structure by a factor of two.⁹ Recent studies,^{10–13} however, have shown that the local, atomic-scale configuration of disordered pyrochlores is better represented by an orthorhombic, weberite-type^{14,15} arrangement (Fig. 1c) instead of a disordered fluorite structure. While

^aDepartment of Nuclear Engineering, University of Tennessee, Knoxville, TN, 37996, USA. E-mail: ericoquinn@utk.edu; mlang2@utk.edu

^bCenter for International Security and Cooperation, Stanford University, Stanford, CA, 94305, USA

^cMechanical and Aerospace Engineering, Oklahoma State University, Stillwater, OK, 74078, USA

^dNeutron Scattering Division, Oak Ridge National Laboratory, Oak Ridge, Tennessee, 37831, USA

^eGSI Helmholtzzentrum für Schwerionenforschung, 64291, Darmstadt, Germany

^fTechnische Universität Darmstadt, 64287, Darmstadt, Germany

† Electronic supplementary information (ESI) available. See DOI: 10.1039/d1ta04924k

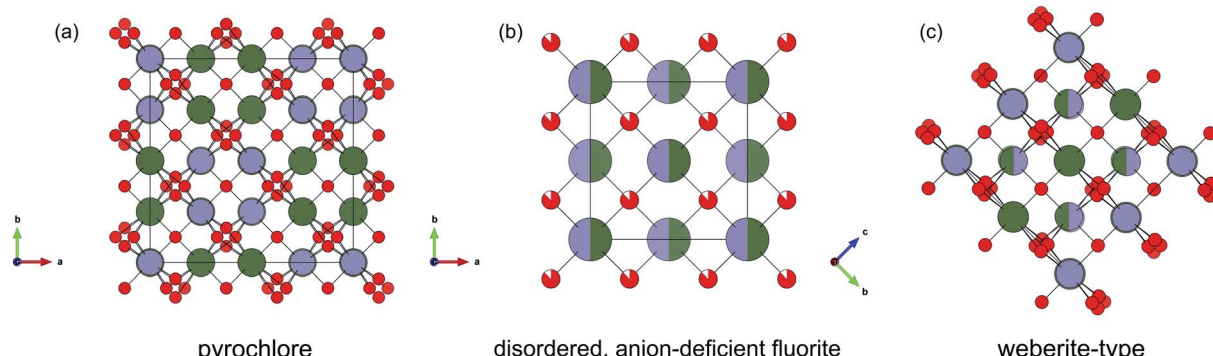


Fig. 1 Atomic arrangement for a single unit cell in the (a) ordered, fluorite-derivative pyrochlore unit cell ($Fd\bar{3}m$) and its structural relationship to the (b) disordered, defect fluorite unit cell ($Fm\bar{3}m$) and the (c) partially-ordered, weberite-type unit cell ($C22\bar{2}1$). The basis vectors for (a) and (b) correspond to the isometric pyrochlore and defect fluorite arrangements while the basis vectors for (c) correspond to the orthorhombic weberite-type arrangement. Green spheres represent Er^{3+} , purple spheres Sn^{4+} , and red spheres O^{2-} . In the defect fluorite and weberite-type phases, cation disorder is represented by spheres filled with two colors. The partially filled red spheres in the defect fluorite phase represent the random distribution of vacant oxygen sites on the anion sublattice.

ordered pyrochlore, disordered fluorite, and weberite-type (Fig. 1) are all derivatives of the parent ideal fluorite structure, each phase has distinct short-range polyhedral configurations.

Among their various applications, pyrochlore oxides have been proposed as durable matrices for the incorporation and immobilization of nuclear wastes. These waste-form materials must be structurally tolerant of self-irradiation from radiological decay of the immobilized actinides.⁸ Insulating materials, like the pyrochlore oxides, can exhibit a variety of responses to energetic ion irradiation. The pyrochlore $\text{Gd}_2\text{Ti}_2\text{O}_7$, for instance, has been shown to undergo a crystalline-to-amorphous transition when doped with ^{244}Cm , which undergoes alpha-decay to emit 1.452 MeV u^{-1} alpha particles.¹⁶ The alpha-decay process of most actinides results in $1.0\text{--}1.5 \text{ MeV u}^{-1}$ alpha particles, alongside relatively heavy, low-energy recoil nuclei (less than 1 keV u^{-1}).¹⁷

Many studies have simulated the response of the pyrochlore structure to alpha-decay recoil nuclei, which deposit energy to a material predominately by ballistic collisions with other nuclei in the lattice, using heavy ion irradiation at keV–MeV energies.^{9,18–21} By contrast, ions with kinetic energy greater than 1 MeV u^{-1} , such as alpha particles, fission fragments, and swift heavy ions deposit energy by electronic excitation of the target material. The deposited energy is transferred to the material via electron-phonon coupling, typically producing a heated (possibly molten) cylindrical region around the ion trajectory in insulating materials. This heating event occurs within a few nanometers of the ion path and lasts for about 100 fs, during which the material is driven far from equilibrium.¹³ This event is followed by a rapid cooling stage in which material modifications are quenched-in, leaving behind a cylindrical ion track of modified material.^{22,23} During this quenching phase, recrystallization may occur at the interface between the molten track core and the surrounding crystalline matrix.²⁴ In some pyrochlore oxides, electronic excitation induced by swift heavy ion irradiation creates tracks with distinct, concentric damage zones^{22,23} (i) an amorphous core closest to the ion trajectory; (ii)

a surrounding disordered, anion-deficient fluorite shell; and (iii) a halo of defect-rich pyrochlore extending farthest outward from the ion path. Interestingly, these three damage zones even appear in ion tracks of pyrochlore materials known to fully amorphize when exposed to high fluences of swift heavy ions, such as the titanate pyrochlores (e.g., $\text{Gd}_2\text{Ti}_2\text{O}_7$).²⁵ This implies that some sample regions are initially transformed into disordered fluorite or defective pyrochlore, then amorphized upon subsequent ion impact.

Prior work has sought to quantitatively model these transformation pathways. The heterogeneous track overlap model (HTOM) developed by Sattonnay *et al.*²⁶ accounts for transformations between pyrochlore, disordered fluorite, and amorphous phases. This model not only reproduced ion-induced phase transformations in amorphizable titanate pyrochlores, but also in zirconate pyrochlores (e.g., $\text{Gd}_2\text{Zr}_2\text{O}_7$), which predominately underwent an order-disorder transformation to the disordered fluorite phase when exposed to 120 MeV U ions. Tracy *et al.*¹³ introduced an alternative damage accumulation model to account for the complex morphology of swift heavy ion tracks (2.2 GeV Au ions) in stannate pyrochlores (e.g., $\text{Gd}_2\text{Sn}_2\text{O}_7$). For $\text{A}_2\text{Sn}_2\text{O}_7$ pyrochlores with larger A-site cations, complete amorphization was induced, while partial amorphization was observed for stannate pyrochlores with smaller A-site cations, even at high ion fluences where extensive track overlap occurs. It was concluded that partial epitaxial recrystallization of amorphous material to disordered fluorite must be considered to accurately model damage accumulation from swift heavy ions and to explain irradiation-induced amorphization that saturates below 100%. Neither model, however, accounts for the halo of defective pyrochlore observed directly with high-resolution electron microscopy²³ and indirectly with coupled X-ray diffraction and Raman spectroscopy.²²

The relative size of ion-induced damage zones and the final structural response to prolonged ion exposure to very high fluences are governed primarily by chemical composition of the pyrochlore compound. Specifically, the radiation response was

previously linked to the ratio of the cationic radii, r_A/r_B .^{22,27,28} As this ratio becomes smaller, the cation antisite defect energy, the basis for an order-disorder transformation, decreases. This can be seen in the contrasting radiation response of $\text{Er}_2\text{Ti}_2\text{O}_7$ and $\text{Er}_2\text{Zr}_2\text{O}_7$. The latter ($r_A/r_B = 1.39$ (ref. 29)), which forms a disordered fluorite phase during synthesis with pre-existing structural disordering of cation and anion sublattices, exhibits no apparent radiation-induced amorphization.³⁰ Conversely, fully ordered $\text{Er}_2\text{Ti}_2\text{O}_7$ pyrochlore ($r_A/r_B = 1.66$) can be readily amorphized by swift heavy ion irradiation.³¹ Based solely on r_A/r_B , it would be expected that $\text{Er}_2\text{Sn}_2\text{O}_7$ ($r_A/r_B = 1.46$) would exhibit an irradiation response intermediate to those of its titanate and zirconate counterparts. However, the nature of chemical bonding may also influence the interatomic forces controlling track formation and relaxation processes, the recrystallization at the track-matrix interface,³² and, thus, the detailed morphology of the induced damage zones. Materials with a high degree of short-range covalent bonding might allow for structural stabilization in different energy minima during ion exposure while systems with largely ionic bonding will be driven by the need to neutralize electrostatic charges via long-range ordering.³³ With an electronegativity of the Sn cation (1.96 in Pauling units) that is much higher than those of Zr (1.33) and Ti (1.54),³⁴ there may be an additional influence of the strong covalent network of Sn–O–Sn chains³⁵ on the radiation response of $\text{Er}_2\text{Sn}_2\text{O}_7$ beyond what is expected based only on the r_A/r_B ratio.

In this paper, we elucidate the phase transformation pathways that a stannate pyrochlore undergoes during swift heavy ion irradiation over all material length scales. We present a systematic characterization of the response of $\text{Er}_2\text{Sn}_2\text{O}_7$ to 2.2 GeV Au ion irradiation using state-of-the-art complementary analytical techniques. Analysis of short- and long-range structural modifications, on both the cation and oxygen sublattices, yielded quantitative information on ion-induced phase changes. The evolution of different phases was analyzed with increasing fluence using available damage accumulation models to gain further insight into the complex morphology of ion tracks in $\text{Er}_2\text{Sn}_2\text{O}_7$ pyrochlore with quantitative information on cross sectional areas of individual damage zones. Based on neutron total scattering experiments, we develop a new model of phase accumulation in irradiated pyrochlores that accounts for the formation of a defective pyrochlore “halo”.

2. Experimental methods

2.1. Synthesis and swift heavy ion irradiation

Poly-crystalline samples of $\text{Er}_2\text{Sn}_2\text{O}_7$ were synthesized by mixing constituent oxides Er_2O_3 and SnO_2 in the proper stoichiometric ratios. After being pressed into pellets and fired for 20 hours at 1200 °C, the powders were reground, repressed, and fired again for 24 hours at 1400 °C. The resulting pellets were reground into a powder with an average grain size of ~1 µm. Samples were prepared for ion irradiation using two different procedures depending on the subsequent characterization technique. For neutron scattering experiments, which require relatively large sample volumes, the powder was compacted using a hydraulic

press to a pressure of 25 MPa into 75 µm deep, 1 cm diameter cylindrical indentations that were machined into thin aluminum plates. These sample holders were then wrapped in 7 µm thick aluminum foil. Four holders were mounted on a 5 cm × 5 cm aluminum plate for a given ion fluence as described in detail elsewhere.^{36,37} For X-ray diffraction and electron microscopy measurements, small $\text{Er}_2\text{Sn}_2\text{O}_7$ wafers of a few mm in diameter were pressed on a die with a hydraulic press using a pressure of 25 MPa, and subsequently fixed onto 1 cm² aluminum support plates.¹³

The sample thickness was limited to 70 µm in the custom aluminum holders (for neutron measurements) and to 40 µm for the wafers (for X-ray and electron measurements). These maximum thicknesses were chosen according to energy loss calculations using the SRIM code,³⁸ in order to isolate the effects of electronic energy loss and to exclude the nuclear collisions that occur close to the end of the ion path. Employing a sample density correction factor introduced by Lang *et al.*,³⁹ the density of each sample in the SRIM calculations was assumed to be 60% of the theoretical density of $\text{Er}_2\text{Sn}_2\text{O}_7$ (8.19 g cm⁻³) which represents the powder packing density typically achieved under cold pressing.⁴⁰ Use of this formulation ensured that the ions (projected range of 90 µm) completely penetrated each sample with negligible nuclear energy loss. Irradiation of all samples was performed with 2.2 GeV Au ions at the beamline X0 of the UNILAC accelerator, at the GSI Helmholtz Centre for Heavy Ion Research in Darmstadt, Germany. A broadly defocused beam with a flux of ~10⁹ ions per sec cm² was used to irradiate samples at room temperature to fluences of 3×10^{11} , 6×10^{11} , 7×10^{11} , 2×10^{12} , 4×10^{12} , 5×10^{12} , and 8×10^{12} ions per cm². The Au ions induced a mean energy loss, dE/dx , in the 40 µm thin sample wafers of 48(1) keV nm⁻¹ (for X-ray diffraction and electron microscopy) and of 47(2) keV nm⁻¹ in the 70 µm thin samples pressed into aluminum holders (for neutron scattering) with the uncertainty describing the variation of dE/dx along the ion path within the samples.

2.2. Transmission electron microscopy (TEM) and X-ray diffraction (XRD) characterization

A small piece of the sample wafer irradiated to a fluence of 3×10^{11} ions per cm² was crushed into a fine powder between two glass slides and subsequently deposited onto a holey-carbon TEM grid. Electron microscopy was used to analyze individual, non-overlapping ion tracks. The sample was oriented such that the electron beam was parallel to the trajectory of the swift heavy ions, allowing for imaging of the track cross-section. High-resolution images of multiple tracks were collected using high-angle annular dark field (HAADF) imaging in a 5th order aberration corrected scanning transmission electron microscope (STEM) (Nion UltraSTEM 200) operating at 200 kV. An electron probe with 28 ± 2 pA current was used in the experiment.

XRD measurements were performed on sample wafers irradiated to 6×10^{11} , 2×10^{12} , 5×10^{12} and 8×10^{12} ions per cm², as well as an unirradiated reference sample at the beamline B2 of the Cornell High Energy Synchrotron Source (CHESS). The

wafers were fixed to the edge of a stripe of tape and analyzed in transmission mode (at a sample location uncovered by the tape) using a 1 mm^2 monoenergetic 25 keV X-ray beam ($\lambda = 0.496\text{ \AA}$) with exposure times of five minutes. Debye diffraction rings were recorded with a Mar CCD detector, and integrated two-dimensional patterns were produced with the software FIT 2d using a CeO_2 calibrant.⁴¹ Patterns collected from different samples were compared by normalizing the intensity of each to the same (strongest) diffraction maximum.

2.3. Neutron total scattering characterization

Neutron total scattering experiments were performed at the Nanoscale-Ordered Materials Diffractometer (NOMAD)⁴² at the Spallation Neutron Source (SNS) at Oak Ridge National Laboratory. Between 75–100 mg of each sample (7×10^{11} , 2×10^{12} , 4×10^{12} , and 8×10^{12} ions per cm^2) was recovered from the custom aluminum holders by scraping with a blunt needle. The material from all 4 holders irradiated to a given fluence was combined, ground into a fine powder, and measured at ambient conditions along with an unirradiated reference sample for about 100 minutes in 2 mm diameter quartz capillaries with a wall thickness of 0.01 mm. Scattering measurements were performed on diamond powder to calibrate the six time-of-flight detectors. Additionally, 60 minutes measurements were collected from a solid vanadium rod and an empty 2 mm quartz capillary. Neutron total scattering structure functions, $S(Q)$, were obtained by normalizing the background-subtracted scattering intensity to the scattering intensity from the vanadium rod (additional details can be found elsewhere^{43,44}). The structure functions were then multiplied by a Lorch function⁴⁵ to dampen data noise at high Q . The structure function was corrected for unphysical curvature with the use of a Fourier filter. Finally, the reduced pair distribution function $G(r)$ was obtained, using the STOG program,⁴⁶ by a Fourier transform in Q :

$$G(r) = \frac{2}{\pi} \int Q[S(Q) - 1] \sin(Qr) dQ \quad (1)$$

where the limits of integration were $Q_{\min} = 0.2\text{ \AA}^{-1}$ and $Q_{\max} = 25.0\text{ \AA}^{-1}$. The integrated term $Q[S(Q) - 1]$ is also known as the “reduced structure function” or $F(Q)$.

The GSAS⁴⁷ software package was used to refine neutron diffraction patterns from NOMAD banks 2–5. The structural parameters for the pyrochlore and disordered fluorite models used are summarized in Table 1. Additional refined parameters include arbitrary scale factors, sample absorption factor, the x position of the $48f$ oxygen atom (pyrochlore), atomic displacement parameters (ADPs) for each Wyckoff equipoint, and a 10 term Chebyshev series as the background. All diffraction pattern refinements resulted in total R_{wp} (goodness-of-fit) values lower than 6.2%. Local structure models were obtained from real-space small-box refinement of the PDFs using PDFgui.⁴⁸ For small-box characterization, a parameter (“delta1”) was refined to account for locally correlated atomic motion. To keep the number of refinable parameters to a minimum, isotropic ADPs were assigned to each Wyckoff equipoint and the same ADP was used for all three $4a$ oxygen sites in the $C222_1$ weberite-type

Table 1 Summary of structural parameters used for Rietveld and small-box refinement. Free positional parameters are in boldface

Wyckoff equipoint (C.N.)	Occupancy	<i>x</i>	<i>y</i>	<i>z</i>
Pyrochlore (<i>Fd3m</i>)				
<i>16d</i>	Er	0.5	0.5	0.5
<i>16c</i>	Sn	0.0	0.0	0.0
<i>48f</i>	O	0.338	0.125	0.125
<i>8b</i>	O	0.125	0.125	0.125
Defect fluorite (<i>Fm3m</i>)				
<i>4a</i>	Er0.5Sn0.5	0.0	0.0	0.0
<i>8c</i>	O	0.25	0.25	0.25
Weberite-type (<i>C222</i>₁, setting 1)				
<i>4b</i>	Sn	0.000	0.0	0.250
<i>8c</i>	Er0.5Sn0.5	0.250	0.250	0.000
<i>4b</i>	Er	0.000	0.500	0.250
<i>8c</i>	O	0.166	0.061	0.147
<i>8c</i>	O	0.120	0.744	0.251
<i>4a</i>	O	0.121	0.500	0.000
<i>4a</i>	O	0.123	0.500	0.500
<i>4a</i>	O	0.131	0.000	0.000

model. All small-box refinements yielded R_{wp} values lower than 11.0%.

To determine the relative fraction of the radiation-induced amorphous phase present at each fluence, the signal in the neutron total scattering structure functions, $S(Q)$, was deconvoluted into contributions from diffuse scattering bands (from the amorphous phase) and diffraction peaks (from the crystalline phases) using the method developed by Lang *et al.*²⁸ The amorphous fraction at each fluence was calculated as the ratio of the integrated intensity of the first-order amorphous band to the total integrated intensity over the same range in Q -space including the crystalline Bragg peaks. Peak analysis was performed with OriginPro 2018.⁴⁹ While this technique has previously been utilized exclusively for X-ray diffraction data, it is also applicable to neutron total scattering data, as the signal corresponding to diffuse scattering by the amorphous phase is not subtracted with the background in the earlier data processing.

3. Results

3.1. Transmission electron microscopy

Individual ion tracks were observed by HAADF/STEM imaging of $\text{Er}_2\text{Sn}_2\text{O}_7$ irradiated to the lowest fluence of 3×10^{11} ions per cm^2 (Fig. 2a). Spatially separated tracks are indicated by circular regions of modified contrast, with respect to the surrounding unirradiated material. As has been observed for other titanate^{22,50,51} and stannate¹³ pyrochlore compositions, the internal structure of ion tracks shows a complex morphology (Fig. 2b) under high-resolution TEM imaging, consisting of an amorphous core (dark contrast) surrounded by a crystalline shell (lighter contrast) and a bright halo region. For previously studied pyrochlore compositions the shell was identified as a disordered, defect-fluorite phase and the halo was explained

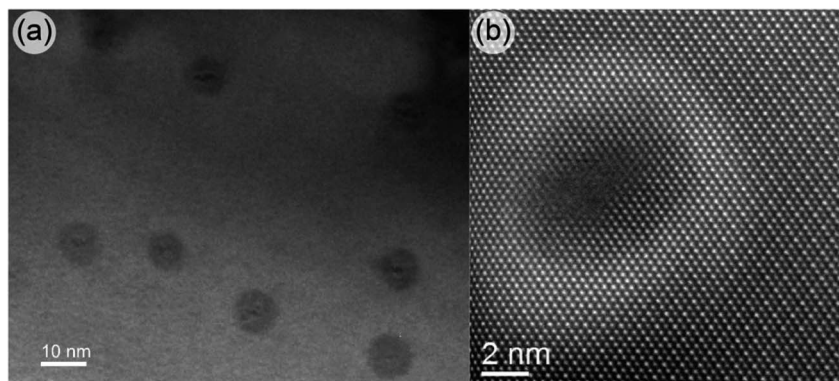


Fig. 2 HAADF/STEM images of 2.2 GeV Au tracks in $\text{Er}_2\text{Sn}_2\text{O}_7$. (a) Bright field image at lower magnification showing individual ion tracks (dark contrast) and (b) high-resolution image revealing that an individual ion track consists of an amorphous core and a crystalline shell, surrounded by a bright contrast region that can be attributed to a defect-rich pyrochlore halo.

by strain from a defective pyrochlore region.^{52–54} The diameter of the innermost amorphous core was determined from high-resolution images to be $3.2(2)$ nm, based on the measurement of five ion tracks along various radial directions (cross-sectional regions are not fully circular). The overall extension of the second damage zone from the track center to the edge of the shell (region of intermediate contrast between amorphous core and bright halo) was determined as $7.2(3)$ nm, and the diameter of the outermost bright halo (track center to edge of halo) was approximated to be $12.6(5)$ nm.

3.2. X-ray diffraction

The synchrotron XRD pattern of the pristine sample reveals a highly crystalline starting material with diffraction maxima indexed unambiguously as pyrochlore (Fig. 3). The most intense Bragg peak, near 2.0 \AA^{-1} , is the $(222)_{\text{PY}}$ pyrochlore phase peak. The $(133)_{\text{PY}}$ pyrochlore superstructure peak, present in ordered pyrochlore but absent in disordered defect fluorite, is clearly visible around 2.6 \AA^{-1} . Increasing the applied ion fluence leads to attenuation of the $(133)_{\text{PY}}$ peak along with other peaks with odd Miller indices (all of which are pyrochlore superstructure peaks), while diffraction maxima with even Miller indices (*e.g.*, $(222)_{\text{PY}}$) undergo a gradual broadening. The decrease in intensity of the pyrochlore superstructure peaks with increasing fluence is explained by an order-disorder transformation to a disordered fluorite phase.⁵⁵ Peak broadening in oxides irradiated with swift heavy ions, as occurs in the remaining peaks, is typically attributed to the accumulation of microstrain accompanying defect production.^{56,57} Irradiation-induced fragmentation and reduction of grain size can be neglected at the fluence range used in this study. At the highest fluence used in this study (8×10^{12} ions per cm^2), a broad diffuse scattering background is apparent beneath the most intense diffraction maximum (1.9 \AA^{-1} to 2.5 \AA^{-1}). Diffuse scattering is indicative of an atomic arrangement that lacks coherency over longer length scales, such as an amorphous phase. While the X-ray data were not further analyzed to extract phase fractions (neutron data was used for this purpose), radiation-induced structural changes evidenced by XRD agree well the track morphology

seen in the TEM images and with the findings of previous work.¹³ Swift heavy ion irradiation of $\text{Er}_2\text{Sn}_2\text{O}_7$ pyrochlore causes the buildup of defects, a transformation to the defect-fluorite structure, and the formation of an amorphous phase.

3.3. Neutron total scattering – long-range structural analysis

In agreement with the XRD results, the neutron diffraction pattern of the unirradiated sample is consistent with a single-

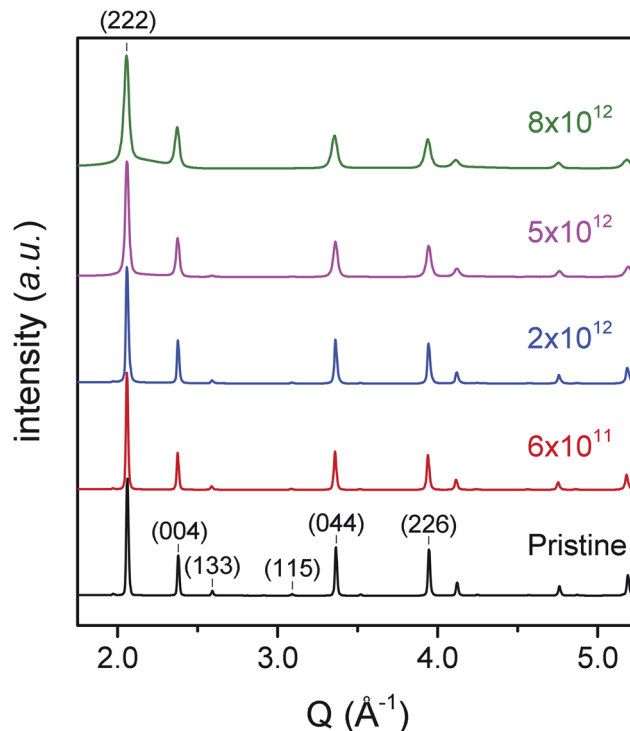


Fig. 3 X-ray diffraction patterns ($1.75 \text{ \AA}^{-1} < Q < 5.25 \text{ \AA}^{-1}$) of $\text{Er}_2\text{Sn}_2\text{O}_7$ before and after irradiation with 2.2 GeV Au ions as a function of increasing fluence. All Bragg peaks have been normalized to the same maximum intensity. The prominent diffraction maxima of the pyrochlore structure are indexed for the XRD pattern of the pristine sample, and the fluence values are given in number of ions per cm^2 .

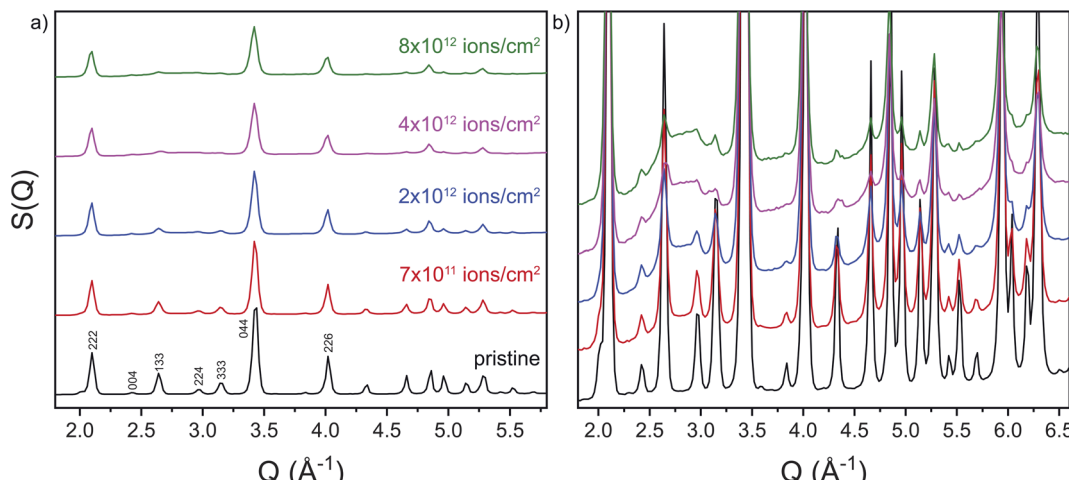


Fig. 4 Neutron total scattering structure functions $S(Q)$ of $\text{Er}_2\text{Sn}_2\text{O}_7$ before and after irradiation with 2.2 GeV Au ions as a function of increasing fluence. Patterns are stacked (a) from $1.75 \text{ \AA}^{-1} < Q < 5.80 \text{ \AA}^{-1}$ and (b) from $1.75 \text{ \AA}^{-1} < Q < 6.60 \text{ \AA}^{-1}$ with a tighter spacing between patterns to more easily see the diffuse scattering contributions. The prominent maxima of the pyrochlore structure are indexed at for the diffraction pattern of the pristine sample, and the fluence values are given in number of ions per cm^2 .

phase fully ordered pyrochlore (Fig. 4a). Rietveld refinement of the neutron diffraction pattern yields a unit-cell parameter of $10.3625(2) \text{ \AA}$ and an oxygen position parameter (x_{48f}) of $0.33725(6)$. The irradiation-induced diffuse scattering increases over a broad range in reciprocal space with increasing fluence (Fig. 4b) beneath and between the Bragg peaks and is already detectable after irradiation to 7×10^{11} ions per cm^2 . The diffuse scattering is more pronounced in the neutron diffraction data as compared to XRD which can be explained by the higher sensitivity of neutron scattering to the oxygen sublattice. Peak deconvolution over a Q -space from 2.25 \AA^{-1} to 3.75 \AA^{-1} (the region of the first-order amorphous diffuse scattering band) could be directly applied to the structure functions to determine the amorphous sample fraction for each fluence following the procedure outlined in.²⁸ This analysis showed that the amorphous phase fraction reaches $28(4)\%$ after irradiation to the maximum fluence of 8×10^{12} ions per cm^2 and the results for all fluences are summarized in Table 2. The intensity of the pyrochlore superstructure Bragg peaks (odd Miller indices) significantly decreases with increasing ion fluence and only low-intensity peaks remain at 8×10^{12} ions per cm^2 (Fig. 4b). This intensity reduction is accompanied by a pronounced peak

broadening. In agreement with the XRD results, Bragg peaks with even Miller indices decrease also in intensity and broaden over the entire fluence range. As is the case for X-ray diffraction, the close structural similarity of the pyrochlore and disordered fluorite diffraction patterns make reliable quantification of the two crystalline phases difficult using long-range data, particularly with an increasing background of diffuse scattering.

3.4. Neutron pair distribution function analysis – intermediate-range structural analysis

Neutron PDF analysis was utilized to characterize the effects of ion irradiation on the short- ($1.5\text{--}15 \text{ \AA}$) and intermediate-range ($15\text{--}50 \text{ \AA}$) structure. Peaks in the PDF arise from atom–atom correlations of mean distance r . The area of a peak is proportional to the number of atomic pairs found at that distance (*i.e.*, coordination number) and the shape and width provide insight into structural disorder. The PDF of the unirradiated sample confirms the presence of pair correlations associated with a fully locally ordered pyrochlore structure (Fig. 5) in agreement with the long-range data (X-ray and neutron diffraction). The low R_w value confirms the excellent agreement between experimental data and structural model with no evidence of any

Table 2 Phase fractions extracted from peak deconvolution (amorphous) and small-box refinement of neutron PDF data ($15\text{--}50 \text{ \AA}$ for disordered fluorite, defective pyrochlore, and pristine pyrochlore and $1.5\text{--}15 \text{ \AA}$ for the weberite-type configuration). The swelling of the unit cell in the defective pyrochlore phase increased from $0.7(3)\%$ at 7×10^{11} ions per cm^2 to $1.3(4)\%$ at 2×10^{12} ions per cm^2 and saturated at $2.0(4)\%$ after exposure to 4×10^{12} ions per cm^2

Fluence (ions per cm^2)	Amorphous	Disordered fluorite	Defective pyrochlore	Pristine pyrochlore	Weberite-type configuration
Pristine	0	0	0	1	0
7×10^{11}	0.12(1)	0.32(9)	0.10(11)	0.46(8)	0.51(4)
2×10^{12}	0.20(1)	0.54(5)	0.06(6)	0.20(2)	0.78(4)
4×10^{12}	0.25(1)	0.61(6)	0.07(5)	0.07(1)	0.93(4)
8×10^{12}	0.28(4)	0.55(9)	0.08(6)	0.08(2)	0.92(4)

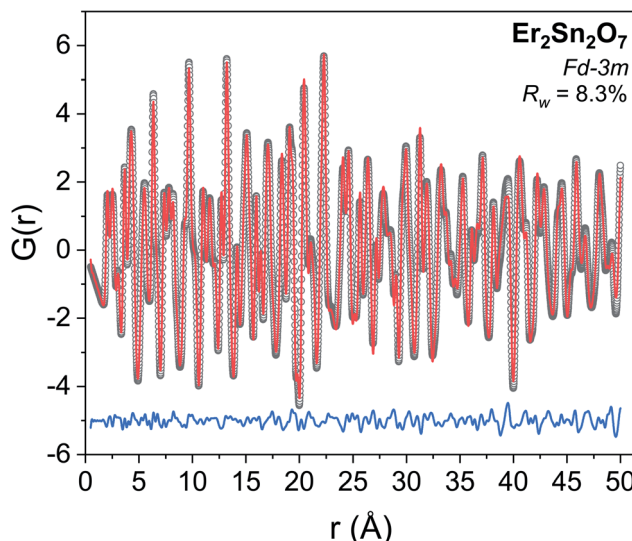


Fig. 5 Neutron PDF obtained for unirradiated $\text{Er}_2\text{Sn}_2\text{O}_7$ pyrochlore (black circles) with small-box refinement fit (red line) and the difference between the two (blue line). The structural model of ideal pyrochlore ($Fd\bar{3}m$) describes the experimental data well over the short- and intermediate range as indicated by a goodness-of-fit parameter (R_w) of 8.3%.

impurity phases. Ordered pyrochlore and disordered fluorite exhibit closely-related diffraction patterns with Bragg peaks at very similar, or even identical, positions in Q -space, but each phase exhibits distinct distributions of pair correlations in r -space (1.5–50 Å). Amorphous materials, by definition, do not exhibit long-range structural periodicity and their atomic correlations only contribute to the short-range structure ($r < 15$ Å). Thus, radiation-induced disordering to fluorite is unambiguously identified by neutron PDF analysis of the intermediate r -range (15–50 Å) with distinct peaks for ordered pyrochlore and disordered fluorite and no contribution from the amorphous phase.

Based on XRD (Fig. 3) and neutron diffraction (Fig. 4) data, irradiation to a fluence of 7×10^{11} ions per cm^2 leaves most of the sample unchanged from its initial pyrochlore phase. Thus, the pyrochlore phase with structural parameters (e.g., unit cell parameter, x_{48f} position) corresponding to the pristine pyrochlore structure was the major component in the PDF small-box refinement of the intermediate range structure together with the disordered fluorite phase (Fig. 6a); however, the overall fit to the data was improved by minor adjustments of structural parameters of the pyrochlore phase (e.g., unit cell parameter, $48f$ oxygen position). This confirms that a defective but ordered pyrochlore phase is present in addition to the pristine pyrochlore matrix, that forms upon swift heavy ion irradiation. The refinement procedure revealed that in the defective pyrochlore phase, both cations and $8b$ oxygen anions are still ordered on their respective Wyckoff equipoints, but some of the $48f$ oxygen anions have been displaced to the previously vacant $8a$ sites. These displacements and the induced oxygen Frenkel defects can explain the observed swelling of the unit cell by 0.7(3)%. This detailed analysis of intermediate range neutron PDF data

confirms the existence of the previously reported defective pyrochlore phase based on TEM, Raman spectroscopy, and XRD measurements,²² and explains the contrast variation in the ion track halo surrounding the defect-fluorite shell in the high-resolution TEM image (Fig. 2b).

For detailed quantitative analysis, the PDFs of all irradiated samples were refined over the intermediate-range (15–50 Å) with three distinct crystalline phases (Fig. 6): (i) pristine pyrochlore, (ii) disordered fluorite, and (iii) irradiation-modified, defective pyrochlore. Phase fractions were obtained at each fluence based on small-box refinements (Table 2), and the refined structural parameters were used to simulate an individual PDF for each phase from 0.1–100 Å. These simulated PDFs were then Fourier transformed to generate the corresponding reduced structure functions for each phase. This procedure was performed for the maximum fluence (Fig. 7) to compare and contrast the individual crystalline phases and qualitatively describe their contributions to the experimental structure function (long-range data), particularly the defective pyrochlore phase with only subtle modifications. A comparison of the pyrochlore structure functions of defective (blue) and pristine (red) phases reveals that irradiation causes a reduced peak intensity at higher Q values (indicative of disorder) and peak shifts to lower Q values (unit-cell expansion). These changes are obscured in the experimental structure function due to the disordering to fluorite and the amorphization process.

The simulated combined structure function of all three crystalline phases (Fig. 7b) was then subtracted from the experimental structure function (Fig. 7a) to isolate the contribution of the amorphous phase (green) and to analyze structural features that are present beyond the diffuse scattering band. The amorphous phase is characterized by an intense diffuse scattering band between 2.25 \AA^{-1} and 3.75 \AA^{-1} (Fig. 7b). The peak-like feature at 4.0 \AA^{-1} , which is in close proximity to the $(113)_{\text{fluorite}}/(226)_{\text{pyrochlore}}$ Bragg peak, may result from incomplete subtraction of the crystalline contributions. However, since the most intense Bragg peak (3.5 \AA^{-1}) is absent in the amorphous structure function, the relatively sharp peak at 4.0 \AA^{-1} could also indicate atomic ordering within the amorphous phase that persists to the long-range structure.

The evolution of all phases extracted from small-box refinements of PDFs from 15–50 Å (pristine pyrochlore, defective pyrochlore, and disordered fluorite) as well as reciprocal-space peak deconvolution (amorphous) are shown in Fig. 8 as a function of increasing ion fluence. The disordered fluorite phase is the highest radiation-induced phase fraction at each ion fluence but appears to saturate or even decrease slightly beyond irradiation to 4×10^{12} ions per cm^2 , while the amorphous phase fraction increases across the entire fluence range studied. The modified, defective pyrochlore exhibits the smallest phase fraction, increasing initially with ion fluence and saturating at higher fluences where ion tracks begin to extensively overlap. The pristine (unmodified) pyrochlore phase decreases distinctly with ion irradiation but saturates at 8% at the maximum fluence (Table 2). This means that about 8% of the sample volume was not covered by the ion beam even at a fluence of 8×10^{12}

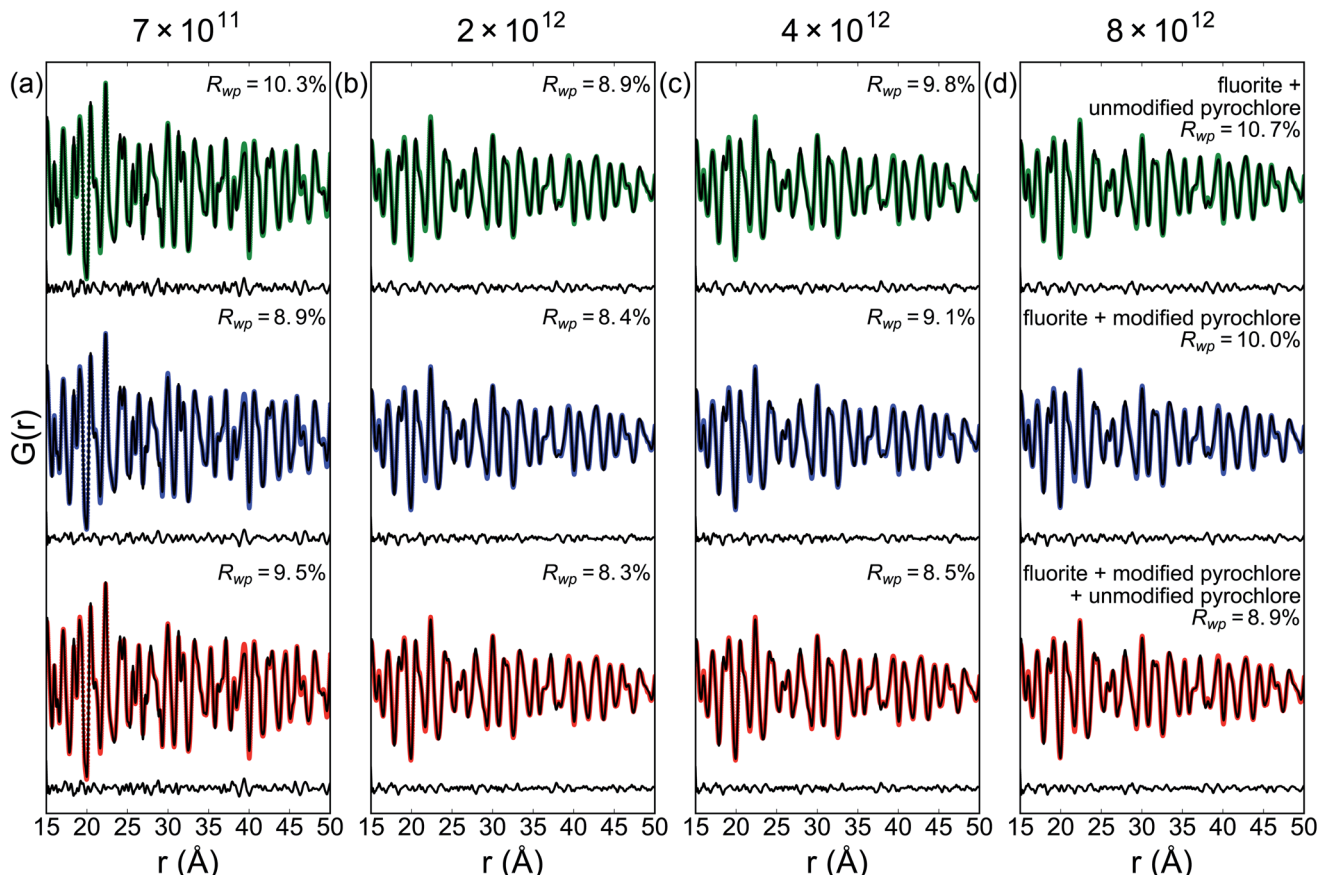


Fig. 6 Neutron PDF data (black curve) with small box refinements of the intermediate-range structure (15–50 Å) for $\text{Er}_2\text{Sn}_2\text{O}_7$ irradiated with (a) 7×10^{11} , (b) 2×10^{12} , (c) 4×10^{12} , and (d) 8×10^{12} ions per cm^2 . Three models were used for the refinement: (top row, green) disordered fluorite plus pristine pyrochlore, (middle row, blue) disordered fluorite plus defective pyrochlore, and (bottom row, red) disordered fluorite plus pristine pyrochlore plus defective pyrochlore. The difference curves (black lines) and the goodness-of-fit values (R_{wp}) are shown below and above the PDFs, respectively. Subfigures (a–d) are shown in more detail in Fig. S1.[†]

ions per cm^2 , which is most likely related to the sample preparation and irradiation procedure. A highly defocused beam was used to irradiate a large area ($5 \text{ cm} \times 5 \text{ cm}$) to obtain a sufficiently large sample mass for neutron characterization. This may have introduced beam inhomogeneities, resulting in incomplete sample coverage by the broad ion beam. Alternatively, pressing powder homogeneously into ultra-thin pellets, with thicknesses of only 10s of μm and areas on the order of 1 cm^2 is very challenging, and some sample regions may have been too thick to be fully penetrated by the ion beam.

3.5. Neutron pair distribution function analysis – short-range structural analysis

To gain further insight into ion beam-induced changes to the local atomic arrangement, the PDFs were also analyzed in the lower r -space region, corresponding to shorter range atomic correlations (Fig. 9). As with the intermediate range PDF, all three crystalline phases contribute to the PDF at this length scale, alongside additional atomic correlations from the amorphous phase. The PDFs show changes with increasing ion fluence across the range between 1.75 \AA and 14.25 \AA with broadening and merging of peaks and changes in intensity

ratios (Fig. 9a). Irradiation-induced modifications in the PDF are particularly pronounced at the level of coordination polyhedra between 1.0 \AA and 3.5 \AA (Fig. 9b). The $\text{Sn}-\text{O}_1$ ($4f$ oxygen site) correlation peak decreases in intensity and shifts to higher r -values, while the $\text{Er}-\text{O}_1$ correlation peak shifts to lower r -values accompanied with a distinct loss in intensity. A new atom-pair correlation emerges after irradiation to 2×10^{12} ions per cm^2 around 2.3 \AA and convolutes with the $\text{Er}-\text{O}_2$ ($8b$ oxygen site) correlation at higher fluences. Interestingly, all PDFs exhibit several isosbestic (crossover) points across all fluences (e.g., at 2.4 \AA and 2.7 \AA), indicating that the probability of finding an atomic pair at a distance at $\sim 2.4 \text{ \AA}$ or $\sim 2.7 \text{ \AA}$ remains unaffected by swift heavy ion irradiation up to the highest fluence (Fig. 9b). One of the isosbestic points, $r \sim 2.7 \text{ \AA}$, is in close proximity to the O_1-O_1 pair correlation distance, and the persistence of this correlation, despite the observed shifts of the cation-anion correlation lengths, may indicate a symmetry reduction caused by the displacement of cations from their ideal positions within coordination polyhedra. This behavior agrees well with previous findings of a weberite-type local atomic arrangement within disordered pyrochlore oxides.¹¹ Small-box refinement of the PDF data confirmed that weberite-type ordering is present in

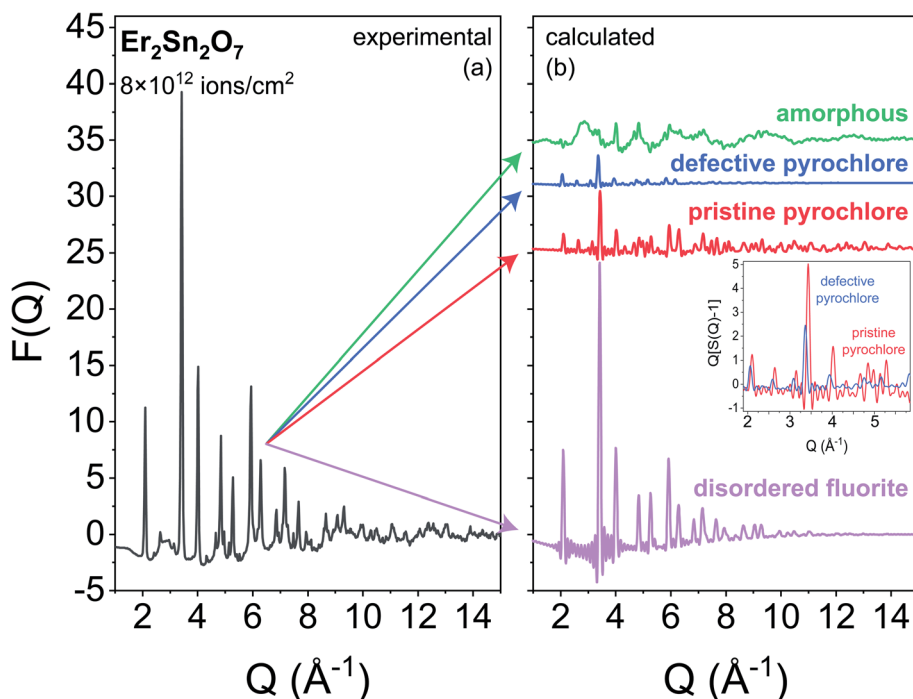


Fig. 7 Reduced neutron structure functions of $\text{Er}_2\text{Sn}_2\text{O}_7$ irradiated with 8×10^{12} ions per cm^2 . (a) Experimental data and (b) simulated from Fourier transform of the individual crystalline phases (pristine pyrochlore, defective pyrochlore, and disordered fluorite) derived from intermediate-range structure refinement of the PDF (Fig. 6), and amorphous contribution from peak deconvolution. Ripples in the baseline of the simulated neutron structure functions arise from the finite Fourier transformations ($r_{\max} = 100 \text{ \AA}$) of the calculated PDFs. Inset shows subtle differences between the pristine (red) and defective (blue) pyrochlore phases such as a shift in position and broadening of peaks indicative of irradiation induced defects.

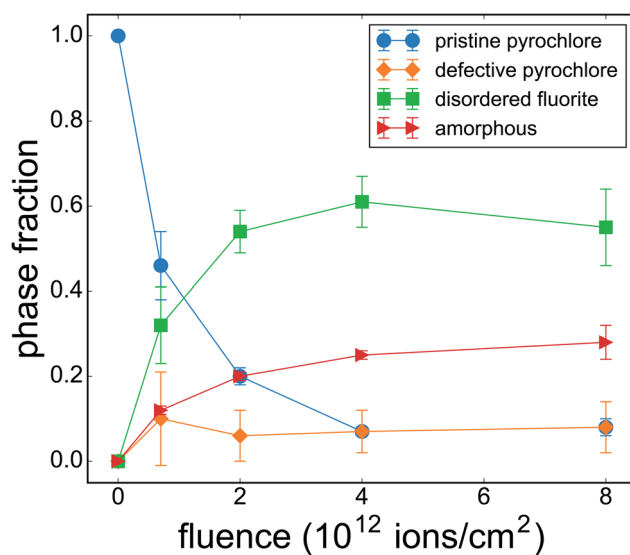


Fig. 8 Weighted phase fractions extracted from small-box refinements of PDFs from 15–50 \AA (pristine pyrochlore, defective pyrochlore, and disordered fluorite) and reciprocal-space peak deconvolution²⁸ (amorphous) as a function of applied ion fluence (Table 2). Uncertainties of the amorphous phase are related to the peak deconvolution process utilized from ref. 28 and uncertainties of the crystalline phases to the small-box refinement of the PDFs. Solid lines are shown to guide the eye.

irradiated $\text{Er}_2\text{Sn}_2\text{O}_7$, but incomplete after irradiation up to 8×10^{12} ions per cm^2 . For example, the prominent correlation peaks in the PDF of unirradiated pyrochlore around 9.5 \AA and 13 \AA (black PDF in Fig. 9a) are still evident up to the maximum fluence (green PDF in Fig. 9a), but they are convoluted into the broad correlations arising from growing disordered sample regions.

As discussed above, the intermediate-range analysis and reciprocal-space peak deconvolution procedure revealed that in total 4 phases are present in each irradiated sample over the fluence range studied (Fig. 8): pristine pyrochlore, defective pyrochlore, disordered fluorite, and amorphous. All of these phases must contribute to the PDF of the short-range structure. It has been previously shown [11] that swift heavy ion irradiated pyrochlore oxides form locally a weberite-type atomic arrangement, independently whether they¹¹ amorphize or disorder to fluorite across the long range. Thus, a two-phase model consisting of pyrochlore ($Fd\bar{3}m$) and weberite-type ($C222_1$)¹¹ was used in the small-box refinement to model the PDFs from 1.5 \AA to 15 \AA as shown in Fig. 10a for the PDF of the sample irradiated to 7×10^{11} ions per cm^2 . Interestingly, the experimental data were accurately described by using just two phases, and the quality of the fit was not affected by the utilized structural model of pyrochlore with fixed (pristine) or adjustable (defective) refined parameters. This implies the weberite-type model captures not only the irradiation-induced atomic-scale modifications associated with disordering and amorphization, but

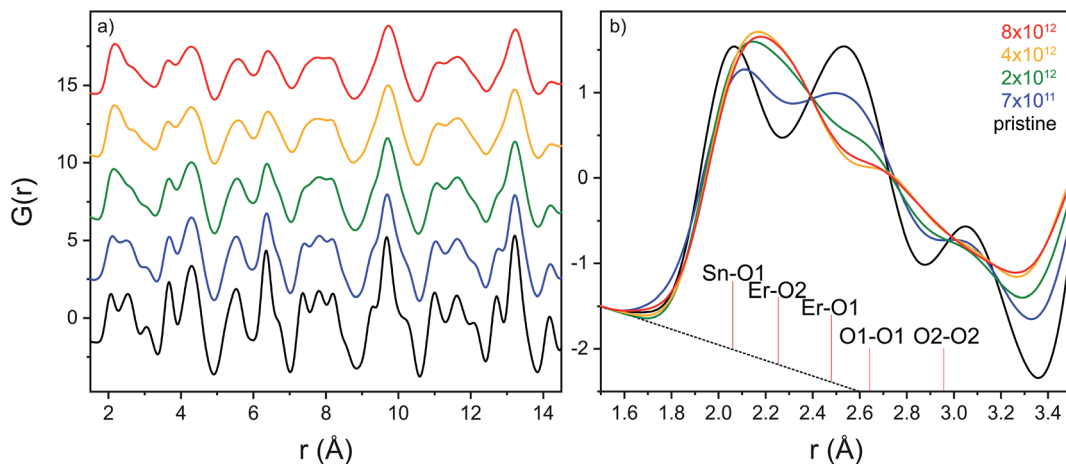


Fig. 9 Stacked neutron pair distribution functions of pristine $\text{Er}_2\text{Sn}_2\text{O}_7$ and irradiated with 2.2 GeV Au ions to different fluences (given in ions per cm^2). The r -value ranges correspond to the (a) local structure between 1.75 Å and 14.25 Å and (b) region of coordination polyhedra. Irradiation distinctly changes the atomic arrangement and pair correlations of pyrochlore (indexed pair correlations in (b) correspond to the pristine sample) to a weberite-type configuration.

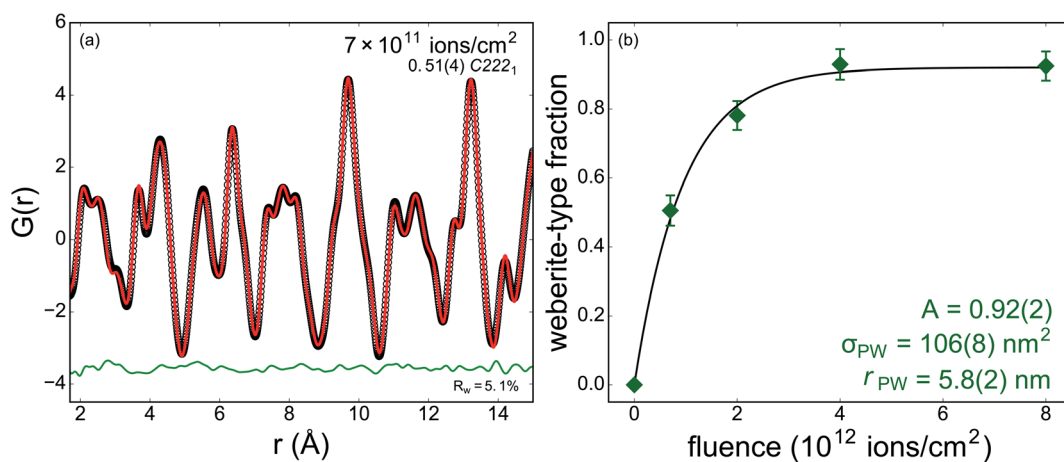


Fig. 10 (a) Representative neutron PDF small-box refinement (1.5–15 Å) of irradiated $\text{Er}_2\text{Sn}_2\text{O}_7$ with the two-phase model consisting of $\text{C}222_1$ weberite-type and pristine $Fd\bar{3}m$ pyrochlore. The black circles correspond to the experimental PDF, the red line is the simulated PDF, and the green line is the difference between the two. (b) Local weberite-type ($\text{C}222_1$) phase fraction obtained by small-box refinement as shown in (a) as a function of ion fluence. The solid line is the fit of a single-impact transformation model (eqn (2)) to the data points with A representing the saturation value, σ_{PW} being the cross section for the pyrochlore-to-weberite transformation and d_{PW} the corresponding diameter (assuming cylindrical symmetry). The error bars of the experimental data are associated with uncertainties of the small-box refinement and the error in the cross section (and diameter) arises from uncertainty of the single-impact model fit to the data points.

also those from the formation of defective pyrochlore. This suggests that defective pyrochlore behaves very similar to disordered fluorite by adopting an atomic arrangement locally that differs from the intermediate- and long-range structure. The weberite-type phase fraction deduced from small-box refinement (Table 2) initially increases linearly with ion irradiation, and saturates at about 0.9 for higher fluence irradiations, consistent with a single-impact mechanism. This means that each individual ion impact directly transforms a region around the ion trajectory from pyrochlore-type to weberite-type (Fig. 10b), but some sample locations are either not hit by the ion beam or some recovery to pyrochlore-type ordering occurs during the quenching process.⁵⁸ The transformation cross-

section, σ_{PW} , for weberite-type phase formation (and associated track radius when assuming cylindrical symmetry) was determined by fitting the following single-impact model:⁵⁸

$$f(\phi) = A(1 - e^{-\sigma_{PW}\phi}) \quad (2)$$

where σ_{PW} is the transformation cross-section of local pyrochlore-type ordering to weberite-type ordering, Φ the ion fluence, and A the dimensionless parameter to account for saturation below unity (0.92(2) in this case). The effective track radius associated with the formation of the weberite-type phase is $r_{PW} = 5.8(2)$ nm. The saturation at 92(2)% transformation to weberite-type with a remaining 8(2)% of pristine pyrochlore is

in excellent agreement with the phase behavior deduced from the intermediate-range structure (Fig. 10 & Table 2). The fact that pristine pyrochlore saturates at this same level after irradiation to a fluence of 8×10^{12} ions per cm^2 across all length scales is, as mentioned above, most likely linked to sample regions that were not covered by the ion beam. This supports further the conclusion from the short-range structural analysis that the local weberite-type ordering is the common atomic arrangement of all ion-induced phases: amorphous, disordered fluorite, and defective pyrochlore.

4. Discussion

4.1 Ion-induced phase accumulation models

Four distinct phases were identified in all irradiated $\text{Er}_2\text{Sn}_2\text{O}_7$ pyrochlore samples based on the long- and intermediate-range structural analysis (Fig. 8), with the phase fraction of each evolving in a complex manner as a function of increasing ion fluence. The corresponding phase fractions were analyzed using two different damage-accumulation models that have been previously proposed for swift heavy ion irradiated pyrochlore oxides. These models, reported by Sattonnay *et al.* and Tracy *et al.*, yield cross-sections for transformation paths identified here and in previous work.^{22,59} Both heterogeneous track-overlap focus on the undamaged pyrochlore matrix, the amorphous track core, and the disordered fluorite shell, but do not consider the defective pyrochlore halo. For example, the model proposed by Sattonnay *et al.*²⁶ assumes the following transformation pathways and associated transformation cross-sections, σ : (i) ordered pyrochlore \rightarrow disordered fluorite (σ_{PD}), (ii) ordered pyrochlore \rightarrow amorphous (σ_{PA}), and (iii) disordered fluorite \rightarrow amorphous (σ_{DA}). The expressions for the pyrochlore (f_{P}), disordered (f_{D}), and amorphous (f_{A}) phase fractions as a function of ion fluence (ϕ) in the Sattonnay *et al.* model are given as:

$$f_{\text{P}}(\phi) = e^{-\phi(\sigma_{\text{PA}} + \sigma_{\text{PD}})} \quad (3a)$$

$$f_{\text{D}}(\phi) = \frac{\sigma_{\text{PD}}e^{-\phi(\sigma_{\text{PA}} + \sigma_{\text{PD}})}[e^{\phi(\sigma_{\text{PA}} + \sigma_{\text{PD}} - \sigma_{\text{DA}})} - 1]}{\sigma_{\text{PA}} + \sigma_{\text{PD}} - \sigma_{\text{DA}}} \quad (3b)$$

$$f_{\text{A}}(\phi) = 1 + \frac{(\sigma_{\text{PA}} - \sigma_{\text{DA}})}{\sigma_{\text{DA}} - \sigma_{\text{PA}} - \sigma_{\text{PD}}} e^{-\phi(\sigma_{\text{PA}} + \sigma_{\text{PD}})} + \frac{\sigma_{\text{PD}}}{\sigma_{\text{DA}} - \sigma_{\text{PA}} - \sigma_{\text{PD}}} e^{-\phi\sigma_{\text{DA}}} \quad (3c)$$

An alternative model was developed by Tracy *et al.*¹³ based on the same core-shell track morphology. The major difference to the model of Sattonnay *et al.*²⁶ is that the disordered fluorite \rightarrow amorphous (σ_{DA}) transformation pathway, which accounts for amorphization by overlapping of defect fluorite shells of two ion tracks, is omitted. Instead, the Tracy *et al.* model includes partial epitaxial recrystallization of some amorphous volume to disordered fluorite, resulting from quenching of an ion track that overlaps with the amorphous core of a previously-produced track. Thus, the cross-section for the formation of the disordered fluorite phase, σ_{D} , includes two pathways: pyrochlore \rightarrow

disordered fluorite and amorphous \rightarrow disordered fluorite. Accounting for recrystallization of the amorphous phase during quenching of an overlapping track can explain the behavior exhibited by many stannate pyrochlore oxides where saturation of the amorphous phase occurs well below 100%.¹³ The expressions for the pyrochlore (f_{P}), disordered fluorite (f_{D}), and amorphous (f_{A}) phase fractions as a function of ion fluence (ϕ) in the Tracy *et al.* model are given as:

$$f_{\text{P}}(\phi) = e^{-\phi(\sigma_{\text{A}} + \sigma_{\text{D}})} \quad (4a)$$

$$f_{\text{D}}(\phi) = \frac{e^{\phi\sigma_{\text{D}}(\sigma_{\text{A}} - \sigma_{\text{D}})}}{\sigma_{\text{A}}e^{\phi\sigma_{\text{A}}} - \sigma_{\text{D}}e^{\phi\sigma_{\text{D}}}} - e^{-\phi(\sigma_{\text{A}} + \sigma_{\text{D}})} \quad (4b)$$

$$f_{\text{A}}(\phi) = \frac{1 - e^{\phi(\sigma_{\text{D}} - \sigma_{\text{A}})}}{1 - \left(\frac{\sigma_{\text{D}}}{\sigma_{\text{A}}}\right)e^{\phi(\sigma_{\text{D}} - \sigma_{\text{A}})}} \quad (4c)$$

The development of these previous models was based primarily on XRD measurements;^{13,26} this technique has limited sensitivity to oxygen anions and thus to subtle changes in the pyrochlore phase such as the production of small defect concentrations. In contrast, the neutron PDF data used here allows, for the first time, to quantify the defective pyrochlore phase as a function of increasing ion fluence. To more comprehensively analyze irradiation-induced phase evolutions in this $\text{Er}_2\text{Sn}_2\text{O}_7$ pyrochlore, the two existing models were expanded by incorporating the transformation pathway from pristine pyrochlore \rightarrow defective pyrochlore (f_{MP}):

$$\frac{df_{\text{MP}}}{d\phi} = \sigma_{\text{MP}}f_{\text{P}} - \sigma_{\text{T}}f_{\text{MP}} \quad (5)$$

where σ_{MP} represents the cross-section for defective pyrochlore formation and σ_{T} equals to $\sigma_{\text{D}} + \sigma_{\text{A}}$ for the model by Tracy *et al.* and to $\sigma_{\text{PD}} + \sigma_{\text{PA}}$ for the model by Sattonnay *et al.* (the total area for transformations to the amorphous and disordered fluorite phases). In this formulation, pristine pyrochlore transforms to defective pyrochlore with each ion impact, while defective pyrochlore regions struck by an ion further disorder to amorphous or disordered fluorite phases. The solution to eqn (5) is:

$$f_{\text{MP}}(\phi) = e^{-\phi(\sigma_{\text{MP}} - \sigma_{\text{T}})}(e^{\phi\sigma_{\text{MP}}} - 1) \quad (6)$$

assuming that the disordered fluorite and amorphous phases form from pyrochlore whether or not it is defective or pristine. This simplification greatly reduces the complexity of each model as the build-up of the amorphous and disordered fluorite phase fractions (eqn (3b), (3c), (4b), and (4c)) remain unchanged from their original descriptions. Both models, expanded by eqn (5), describe well the phase behavior of $\text{Er}_2\text{Sn}_2\text{O}_7$ induced by 2.2 GeV Au ions (Fig. 11) up to the highest fluence accurately accounting for the evolution of all three irradiation-induced phases (only small deviations of model and data points are apparent in Fig. 11). The saturation of the defective pyrochlore phase at higher fluences suggests a recovery pathway from either the amorphous phase, or disordered fluorite phase, or both; this pathway was not included to avoid over-

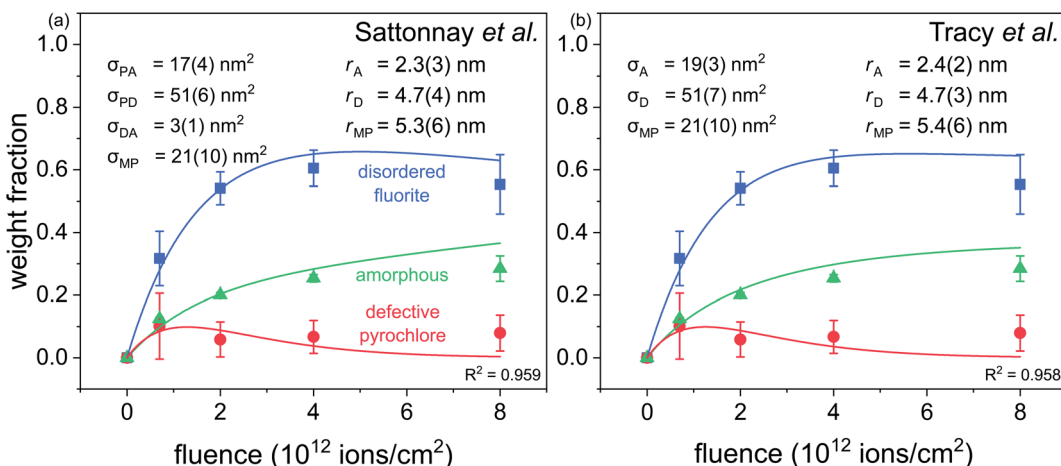


Fig. 11 Radiation-induced fractions of disordered fluorite (blue), amorphous phase (green), and defective pyrochlore (red) deduced from small-box refinements of neutron PDFs from 15–50 Å (crystalline phases) and reciprocal-space peak deconvolution (amorphous phase) as a function of applied ion fluence. The lines are fits to the data utilizing damage-accumulation models developed by (a) Sattonnay *et al.*²⁶ and (b) Tracy *et al.*¹³ with small modifications based on results from this study. Both models consider different phase fractions simultaneously and provide cross-sections, σ , and track diameters, d , for individual damage zones based on eqn (3), (4), and (6). Abbreviations denote to pyrochlore-to-amorphous (PA and A), pyrochlore-to-disordered fluorite (PD), pyrochlore-to-disordered fluorite as well as amorphous-to-disordered fluorite (D), disordered fluorite-to-amorphous (DA), and pristine pyrochlore-to-disordered pyrochlore (MP). R^2 is the coefficient of determination of each model to the phase fractions.

parametrization of our model but could be a focus of future studies on materials with less complex track morphologies.

4.2 Ion-track morphology

The internal structure of a swift heavy ion track in $\text{Er}_2\text{Sn}_2\text{O}_7$ is directly evident by high-resolution TEM images (Fig. 2b) displaying a complex damage morphology consisting of an amorphous core, which is surrounded by a disordered fluorite shell that is surmounted by a defective pyrochlore halo. Indirect information on the size of the different damage zones is available by cross-sections, σ , deduced from track-overlap models fitted to fluence-dependent phase fraction data (Fig. 11). To

compare the size of the different damage zones from TEM and neutron measurements, it is important to define what these values mean and how they are used. For example, the cross-section of the disordered shell, σ_D , describes an area per ion impact that is associated with the formation of disordered fluorite. For example, the cross-section of the amorphous core, σ_A , describes an area per ion impact that is associated with the formation of the amorphous phase. By assuming cylindrical track geometry, which is valid based on TEM investigations (Fig. 2b), with $\sigma_A = \pi(r_A)^2$ the effective radius, r_A , of the amorphous core can be determined. With knowledge of the core-shell morphology and the existence of an inner amorphous

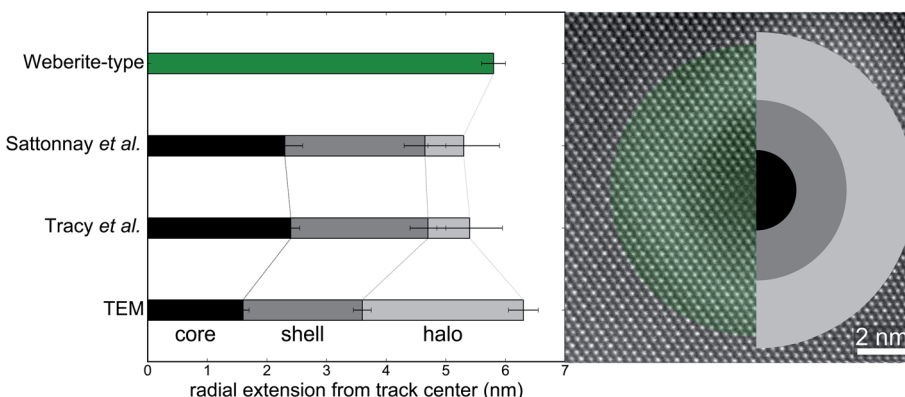


Fig. 12 Summary of the radial extension of different damage regions (core, shell, and halo) within swift heavy ion tracks in $\text{Er}_2\text{Sn}_2\text{O}_7$ based on TEM imaging and neutron total scattering analysis. Error bars in TEM measurements represent the standard error of the mean, and error bars from PDF analysis represent the propagation of uncertainties associated with structural refinement and subsequent fitting procedures with transformation models. The schematic drawings of ion track cross-sections (right) are to scale and display the three distinct long-range damage zones from TEM and neutron analysis consisting of an amorphous core (darkest contrast, inner circular area), a disordered fluorite shell (brighter contrast, intermediate circular area), and a defective pyrochlore halo (brightest contrast, outer circular area) as well as (left) the homogeneous damage morphology across the local structure represented by a weberite-type atomic arrangement (green).

Table 3 Radial extent of the three concentric damage zones induced by 2.2 GeV Au ions in $\text{Er}_2\text{Sn}_2\text{O}_7$ pyrochlore. The top value is the effective radius of the phase (in nm) from the track center and the bottom value in angular brackets is the cross section of the phase (in nm^2)

Phase	TEM	Neutron PDF (15–50 Å) (Tracy <i>et al.</i>)	Neutron PDF (15–50 Å) (Sattonnay <i>et al.</i>)	Neutron PDF (1.5–15 Å)
Core (amorphous)	1.6(1) <8(1)>	2.4(2) <19(3)>	2.3(3) <17(4)>	—
Shell (disordered fluorite)	3.6(2) <33(5)>	4.7(3) <51(7)>	4.7(4) <51(6)>	—
Halo (defective pyrochlore)	6.3(3) <84(12)>	5.4(6) <21(10)>	5.3(6) <21(10)>	—
Total	6.3(3) <125(18)>	5.4(6) <91(20)>	5.3(6) <89(20)>	5.8(2) <106(8)>

region with radius, r_A , the effective radius of the disordered fluorite shell from the track center is given by $(\sigma_A + \sigma_D) = \pi(r_D)^2$. This approach was used to determine radius of each damage zone based on cross-sections from both track-overlap models (Section 4.1), and these values were compared to direct observation from TEM images (Fig. 12 and Table 3).

The inner track core consists of amorphized material that results from the extremely high energy density induced along the ion path (falling off as $1/r^2$ in the radial direction, normal to the track⁶⁰). As shown graphically in Fig. 12, the radius of the amorphous core obtained from TEM images is 1.6(1) nm (Fig. 2b), smaller than the values deduced from the modified track-overlap models of Sattonnay *et al.* ($r_{PA} = 2.3(3)$) and Tracy *et al.* ($r_A = 2.4(2)$). The peak deconvolution method utilized to quantify amorphous phase fractions from X-ray diffraction patterns²⁸ has been previously shown to underestimate the amount of amorphous phase within ion tracks.^{13,61} This is in contrast to the larger radii obtained in the present work where the same deconvolution method was applied to neutron total scattering data. The discrepancy can be explained by the much higher sensitivity of neutron probes to the oxygen sublattice (in contrast to X-rays or electrons). The radial extent of the amorphous core as measured by TEM analysis reflects predominantly the structural aperiodicity of the cations. The larger core radius extracted from neutron data could mean that the loss of long-range coherency occurs on the oxygen sublattice over a larger area than it does on the cation sublattice. This agrees well with the results of a previous study on swift heavy ion irradiated CeO_2 that reported the formation of oxygen defects at radial distances from the track center much greater than the diameter of the ion track as identified by TEM.⁶² On the other hand, the discrepancy between neutron and TEM measurements may be related to the very high sensitivity of neutron probes to diffuse scattering which is already apparent after irradiation to only 7×10^{11} ions per cm^2 (Fig. 4b). Both the disordered fluorite and the amorphous phase contribute to the growing background underneath the Bragg peaks as a result of weberite-type ordering.¹¹ Since the amorphous phase fraction was determined by deconvolution of the experimental structure function, with contributions from all other phases, including disordered fluorite, the obtained values are likely an overestimation across the entire fluence range. This explains the about 50% larger amorphous core radius from neutron measurements as compared with TEM observation (Fig. 12).

The effective radius, r_D , of the disordered fluorite shell was determined by TEM to be 3.6(2) nm (Fig. 2b). This agrees well to

the values deduced from neutron data of 4.7(4) nm for the Sattonnay *et al.* model and 4.7(3) nm for the Tracy *et al.* model. It is challenging to accurately discriminate between the pyrochlore and disordered fluorite structure based on refinement of long-range data due to their highly similar diffraction patterns (for both X-rays and neutrons). This becomes even more difficult with increasing contributions of the amorphous phase to the patterns at higher fluences. The approach presented here, to quantify both phases based on their intermediate-range structure, thus presents a significant improvement. Each phase has a unique signature across this length scale without interference from the amorphous phase that contributes intensity only to the short-range structure (<15 Å). Quantification of the disordered fluorite phase fraction based on this improved assessment yields a cross-section (and corresponding diameter) when fitted with the two track-overlap models, σ_{PD} and σ_D , which is in excellent agreement with the TEM data.

A defective pyrochlore halo has been previously proposed based on its strain contrast in TEM images and its contribution to Raman spectra.^{18,22} A distinct strain contrast around the disordered shell is also observable in the high-resolution TEM images of this study (Fig. 2b) with an effective radius, r_H , of about 6.3(3) nm. The high sensitivity to oxygen and the ability to analyze the intermediate-range structure allowed for additional characterization of the defective pyrochlore halo by neutron measurements. The heterogeneous track-overlap models of Sattonnay *et al.* and Tracy *et al.* were expanded to include this third, outermost damage zone (eqn (6)), and the analysis of the fluence-dependent phase fraction resulted in a radius of the track halo radius of 5.3(6) nm and 5.4(6) nm for the Sattonnay *et al.* model and the Tracy *et al.* model, respectively. These values are smaller than the one obtained from TEM analysis. It remains unclear how the strain contrast in TEM images is related to the underlying defects, and the more direct assessment of the defective pyrochlore phase by neutron probes should be more reliable. This is supported by previous Raman measurements of $\text{Gd}_2\text{Zr}_{2-x}\text{Ti}_x\text{O}_7$ pyrochlores irradiated with 1.43 GeV Xe which reported a halo thickness of about 1 nm.²² Independently of size of the halo, alongside TEM and Raman spectroscopy characterization, the neutron data reported here present an independent confirmation of the existence of such a defective pyrochlore region beyond the defect-fluorite shell.

4.3 Local structure of irradiated pyrochlore

While the long-range structural analysis (neutron scattering and TEM) indicated the presence of 3 distinct damage zones within

the swift heavy ion tracks, characterization of the short-range structure provides a rather different picture. Small-box refinement of PDFs in the region of 1.5–15 Å confirmed the formation of a weberite-type short-range phase in $\text{Er}_2\text{Sn}_2\text{O}_7$ after irradiation with 2.2 GeV Au ions. The weberite-type phase fraction increases with ion fluence consistent with a single-impact model (Fig. 10), and the corresponding track radius (r_{PW}) is 5.8(2) nm. This value agrees well with the total track radii (core + shell + halo) of 5.3(6) nm and 5.4(6) nm based on the Sattonnay *et al.* and Tracy *et al.* models, respectively. This implies that all three damage zones that are produced within swift heavy ion tracks are characterized by the same weberite-type atomic arrangement. This agrees well with previous neutron total scattering studies on pyrochlore oxides with short- and long-range structural characterization. It was shown that both the disordered fluorite structure and the amorphous phase that are observed after ion irradiation across the long range are best described locally by the same weberite-type phase¹¹ and, further, that chemically-induced disorder, that maintains the long-range pyrochlore phase but introduces high concentrations of anion Frenkel defects, also locally yields a short-range weberite-type atomic arrangement.⁶³

The complex ion-track morphology exhibited over the long-range structure appears to be a general phenomenon for pyrochlore oxides.^{18,23,25,64–68} The relative size of core and shell regions depends on the chemical composition²³ and the deposited energy loss of the swift heavy ions.²³ There are currently two explanations for the formation of the disordered fluorite shell: (i) it forms around the amorphous core directly during ion impact within a region where the induced energy density is below the critical value required for amorphization but is sufficient for disordering; or (ii) it forms from a molten region within an ion track during quenching as a result of partial recrystallization at the periphery of the melt. Combined thermal spike and molecular dynamics (MD) simulations^{23,65,69} suggest that process (ii) is more likely and that the shell is the result of epitaxial recrystallization. This is supported by the neutron characterization of samples irradiated to very high fluences which show that the amorphous fraction saturates well below 100% as shown in Fig. 8 (also reported for other stannate pyrochlore oxides¹³). This can only be explained by a disordered fluorite shell that forms repeatedly during each ion impact as a result of recrystallization, regardless of whether or not the initial phase in the region of the ion path is crystalline or amorphous. The short-range analysis through neutron PDF data and the existence of a weberite-type local phase for both the amorphous core and disordered shell supports this track-formation behavior. As previously derived from fundamental chemical rules,¹⁵ $\text{A}_2\text{B}_2\text{O}_7$ pyrochlore oxides commonly adopt a weberite-type atomic arrangement when a fully ordered structure can no longer be maintained due to intrinsic or extrinsic perturbances.¹¹ If one assumes that the same weberite-type coordination polyhedra persist within the molten state, then the amorphous core and disordered fluorite shell represents both the frozen-in or quenched atomic arrangement after ion impact. The temperature profile decreases steeply from the center line of the track radially outward, and the resulting lower quench rate in the outer track region and the interface with the surrounding pyrochlore matrix likely allows for some long-range recrystallization to

occur, yielding the crystalline, but disordered shell. For sample regions that are radially even further away from the ion path the quench rate is again reduced and may be low enough for long-range ordering to pyrochlore with some remnant defect concentrations. This explains the existence of a defective pyrochlore halo as outermost concentric damage region. The homogeneous track morphology at the short-range with a weberite-type atomic arrangement present for all three damage zones supports the scenario that the track halo was originally part of the molten track that formed also the amorphous core and disordered shell. Further experimental and modelling studies are needed to further refine the track-formation mechanism in pyrochlore oxides and to clarify the origin of the defective pyrochlore halo.

5. Conclusions

Complementary characterization techniques (direct characterization by TEM and indirect characterization by X-ray and neutron total scattering) performed over a range of ion fluences provide a comprehensive picture of phase evolution and track morphology for $\text{Er}_2\text{Sn}_2\text{O}_7$ pyrochlore irradiated with 2.2 GeV Au ions. Individual ion tracks consist of an amorphous core, surrounded by a disordered fluorite shell, itself surrounded by a defective pyrochlore halo. With high sensitivity to the oxygen sublattice and the ability of short-range analysis, neutron total scattering provided further structural insight into all three irradiation-induced phases. Characterization of the disordering process over the intermediate-range structure by means of neutron pair distribution functions allowed for accurate quantification of the thickness of the disordered fluorite shell. Comparison with the shell thickness obtained by direct TEM measurement yielded excellent agreement among the two characterization techniques, which presents an improvement over previous diffraction-based investigations and associated challenges of the structurally highly related pyrochlore and disordered fluorite. Neutron characterization provided also clear evidence of a defective pyrochlore phase that was previously only indirectly observed by TEM as strain contrast within a track halo region. The phase fraction of defective pyrochlore was quantified for each ion fluence and considered to accurately describe the damage accumulation process. Existing heterogeneous track-overlap models proposed by Sattonnay *et al.*²⁶ and by Tracy *et al.*¹³ were expanded by addition of a pyrochlore → defective pyrochlore transformation pathway. This improved the modeling of fluence-dependent behavior for all irradiation-induced phases and yielded the size of the defective pyrochlore halo which was only 50% of the size as suggested by TEM measurements. Oxygen Frenkel defects were shown to be an important component of the track halo which explains the challenges of characterization using X-ray and electron probes. Neutron characterization is very sensitive to diffuse scattering, which facilitates the analysis of irradiation-induced amorphization; however, the formation of defects and disorder also contributes to the diffuse scattering and the deduced diameter of the amorphous core is likely an upper bound as supported by the smaller track core from TEM measurements.

Analysis of radiation effects across the short-range structure revealed an atomic-scale transformation from pyrochlore to

weberite-type ($C222_1$), in agreement with previous studies. No other irradiation-induced structural modification was evident from real-space analysis of the local structure ($r < 15 \text{ \AA}$). The weberite-type phase accumulation as a function of ion fluence exhibited behavior consistent with a single-impact mechanism and the resulting track diameter is in very good agreement to the overall track size (core + shell + halo) derived from characterization of the intermediate-range (neutron scattering) and long-range (TEM) structural modifications. This implies that all three damage zones share the same local weberite-type polyhedra, despite their distinct longer-range structure. Thus, the expression of the swift heavy ion track morphology in $\text{Er}_2\text{Sn}_2\text{O}_7$ (and most likely also in other pyrochlore oxides) strongly depends on the length scales considered. The long-range structure as seen in TEM images is heterogeneous with three distinct concentric damage zones. In clear contrast, tracks are fully homogeneous if the short-range structure is considered. It is well established that the characterization of radiation damage, and particularly track size and morphology, strongly depends on the utilized analytical probes and their interaction mechanisms with the target material.²² This study further expands this view and shows that the length-scale over which damage is probed is an important component that must be considered.

Conflicts of interest

There are no conflicts to declare.

Acknowledgements

This work was supported by the U.S. Department of Energy, Office of Science, Basic Energy Sciences under Award #DE-SC0020321. W. F. C. was funded by an Integrated University Program Graduate Fellowship. The electron microscopic data acquisition in this research was conducted at the Center for Nanophase Materials Sciences, which is a DOE Office of Science User Facility. This research at ORNL's Spallation Neutron Source was sponsored by the Scientific User Facilities Division, Office of Basic Energy Sciences, US Department of Energy. The results presented here are based on a UMAT experiment, which was performed at the X0-beamline of the UNILAC at the GSI Helmholtzzentrum für Schwerionenforschung, Darmstadt (Germany) in the frame of FAIR Phase-0. This work is based upon research conducted at the Cornell High Energy Synchrotron Source (CHESS) which is supported by the National Science Foundation and the National Institutes of Health/National Institute of General Medical Sciences under NSF Award No. DMR-1332208. The authors express their appreciation to Devon Drey (University of Tennessee) for thoughtful discussion and technical support and anonymous reviewers for constructive remarks which improved this manuscript.

References

- K. Matsuhira, M. Tokunaga, M. Wakushima, Y. Hinatsu and S. Takagi, *J. Phys. Soc. Jpn.*, 2013, **82**, DOI: 10.7566/JPSJ.82.023706.
- D. P. Leusink, F. Coneri, M. Hoek, S. Turner, H. Idrissi, G. Van Tendeloo and H. Hilgenkamp, *APL Mater.*, 2014, **2**, 032101.
- H. Yan, O. Benton, L. Jaubert and N. Shannon, *arXiv*, 2013, 1–31.
- M. Pirzada, R. W. Grimes, L. Minervini, J. F. Maguire and K. E. Sickafus, *Solid State Ionics*, 2001, **140**, 201–208.
- M. Hanawa, Y. Muraoka, T. Tayama, T. Sakakibara, J. Yamaura and Z. Hiroi, *Phys. Rev. Lett.*, 2001, **87**, 187001.
- J. Zhang, J. Lian, A. F. Fuentes, F. Zhang, M. Lang, F. Lu and R. C. Ewing, *Appl. Phys. Lett.*, 2009, **94**, DOI: 10.1063/1.3155855.
- M. a Subramanian, G. Aravamudan and G. V. S. Rao, *Solid State Chem.*, 1983, **15**, 55–143.
- R. C. Ewing, W. J. Weber and J. Lian, *J. Appl. Phys.*, 2004, **95**, 5949–5971.
- S. Wang, L. Wang, R. Ewing, G. Was and G. Lumpkin, *Nucl. Instrum. Methods Phys. Res., Sect. B*, 1999, **148**, 704–709.
- J. Shamblin, M. Feygenson, J. Neufeld, C. L. Tracy, F. Zhang, S. Finkeldei, D. Bosbach, H. Zhou, R. C. Ewing and M. Lang, *Nat. Mater.*, 2016, **15**, 507–511.
- J. Shamblin, C. L. Tracy, R. I. Palomares, E. C. O'Quinn, R. C. Ewing, J. Neufeld, M. Feygenson, J. Behrens, C. Trautmann and M. Lang, *Acta Mater.*, 2018, **144**, 60–67.
- J. M. Solomon, J. Shamblin, M. Lang, A. Navrotsky and M. Asta, *Sci. Rep.*, 2016, **6**, 1–10.
- C. L. Tracy, J. Shamblin, S. Park, F. Zhang, C. Trautmann, M. Lang and R. C. Ewing, *Phys. Rev. B: Condens. Matter Mater. Phys.*, 2016, **94**, 1–11.
- L. Cai and J. C. Nino, *Acta Crystallogr., Sect. B: Struct. Sci.*, 2009, **65**, 269–290.
- E. C. O'Quinn, K. E. Sickafus, R. C. Ewing, G. Baldinozzi, J. C. Neufeld, M. G. Tucker, A. F. Fuentes, D. Drey and M. K. Lang, *Sci. Adv.*, 2020, **6**, 1–8.
- W. J. Weber, J. W. Wald and H. Matzke, *Mater. Lett.*, 1985, **3**, 173–180.
- Z. Zhixiang, *AIP Conf. Proc.*, 2005, **769**, 1089–1091.
- M. Lang, F. Zhang, J. Zhang, J. Wang, J. Lian, W. J. Weber, B. Schuster, C. Trautmann, R. Neumann and R. C. Ewing, *Nucl. Instrum. Methods Phys. Res., Sect. B*, 2010, **268**, 2951–2959.
- S. X. Wang, B. D. Begg, L. M. Wang, R. C. Ewing, W. J. Weber and K. V. G. Kutty, *J. Mater. Res.*, 1999, **14**, 4470–4473.
- S. X. Wang, L. M. Wang, R. C. Ewing and K. V. Govindan Kutty, *MRS Proc.*, 1998, **540**, 355.
- B. D. Begg, N. J. Hess, W. J. Weber, R. Devanathan, J. P. Icenhower, S. Thevuthasan and B. P. McGrail, *J. Nucl. Mater.*, 2001, **288**, 208–216.
- M. Lang, J. Lian, J. Zhang, F. Zhang, W. J. Weber, C. Trautmann and R. C. Ewing, *Phys. Rev. B: Condens. Matter Mater. Phys.*, 2009, **79**, 1–9.
- M. Lang, M. Toulemonde, J. Zhang, F. Zhang, C. L. Tracy, J. Lian, Z. Wang, W. J. Weber, D. Severin, M. Bender, C. Trautmann and R. C. Ewing, *Nucl. Instrum. Methods Phys. Res., Sect. B*, 2014, **336**, 102–115.

- 24 J. Lian, X. T. Zu, K. V. G. Kutty, J. Chen, L. M. Wang, R. C. Ewing and R. C. Ewing, *Phys. Rev. B: Condens. Matter Mater. Phys.*, 2002, **66**, 541081–541085.
- 25 J. Shamblin, C. L. Tracy, R. C. Ewing, F. Zhang, W. Li, C. Trautmann and M. Lang, *Acta Mater.*, 2016, **117**, 207–215.
- 26 G. Sattonnay, C. Grygiel, I. Monnet, C. Legros, M. Herbst-Ghysel and L. Thomé, *Acta Mater.*, 2012, **60**, 22–34.
- 27 K. Trachenko, *J. Phys.: Condens. Matter*, 2004, **16**, R1491–R1515.
- 28 M. Lang, F. X. Zhang, R. C. Ewing, J. Lian, C. Trautmann and Z. Wang, *J. Mater. Res.*, 2009, **24**, 1322–1334.
- 29 R. D. Shannon, *Acta Crystallogr., Sect. A: Cryst. Phys., Diffr. Theor. Gen. Crystallogr.*, 1976, **32**, 751–767.
- 30 K. E. Sickafus, L. Minervini, R. W. Grimes, J. A. Valdez, M. Ishimaru, F. Li, K. J. McClellan and T. Hartmann, *Science*, 2000, **289**, 748–751.
- 31 C. K. Chung, E. C. O’Quinn, J. C. Neufeind, A. F. Fuentes, H. Xu, M. Lang and A. Navrotsky, *Acta Mater.*, 2019, **181**, 309–317.
- 32 H. M. Naguib and R. Kelly, *Radiat. Eff.*, 1975, **25**, 1–12.
- 33 G. R. Lumpkin, M. Pruneda, S. Rios, K. L. Smith, K. Trachenko, K. R. Whittle and N. J. Zaluzec, *J. Solid State Chem.*, 2007, **180**, 1512–1518.
- 34 A. L. Allred, *J. Inorg. Nucl. Chem.*, 1961, **17**, 215–221.
- 35 T. Ikeda, *Jpn. J. Appl. Phys.*, 1999, **38**, 93.
- 36 M. Lang, C. L. Tracy, R. I. Palomares, F. Zhang, D. Severin, M. Bender, C. Trautmann, C. Park, V. B. Prakapenka, V. a. Skuratov and R. C. Ewing, *J. Mater. Res.*, 2015, **30**, 1366–1379.
- 37 R. I. Palomares, J. Shamblin, C. L. Tracy, J. Neufeind, R. C. Ewing, C. Trautmann and M. Lang, *J. Mater. Chem. A*, 2017, **5**, 12193–12201.
- 38 J. F. Ziegler, M. D. Ziegler and J. P. Biersack, *Nucl. Instrum. Methods Phys. Res., Sect. B*, 2010, **268**, 1818–1823.
- 39 M. Lang, F. Zhang, J. Zhang, C. L. Tracy, A. B. Cusick, J. Vonehr, Z. Chen, C. Trautmann and R. C. Ewing, *Nucl. Instrum. Methods Phys. Res., Sect. B*, 2014, **326**, 121–125.
- 40 E. Luther, C. Necker, B. Mihaila, P. Papin and D. Guidry, *Trans. Am. Nucl. Soc.*, 2011, **104**, 257–258.
- 41 A. P. Hammersley, *J. Appl. Crystallogr.*, 2016, **49**, 646–652.
- 42 J. Neufeind, M. Feygenson, J. Carruth, R. Hoffmann and K. K. Chipley, *Nucl. Instrum. Methods Phys. Res., Sect. B*, 2012, **287**, 68–75.
- 43 M. T. Dove, M. G. Tucker and D. a. Keen, *Eur. J. Mineral.*, 2002, **14**, 331–348.
- 44 E. C. O’Quinn, J. L. Bishop, R. Sherrod, J. Neufeind, S. M. Montemayor, A. F. Fuentes and M. Lang, *J. Mater. Sci.*, 2018, **53**, 13400–13410.
- 45 A. K. Soper and E. R. Barney, *J. Appl. Crystallogr.*, 2012, **45**, 1314–1317.
- 46 M. G. Tucker, D. A. Keen, M. T. Dove, A. L. Goodwin and Q. Hui, *J. Phys.: Condens. Matter*, 2007, **19**, DOI: 10.1088/0953-8984/19/33/335218.
- 47 A. C. Larson, *Los Alamos Natl. Lab., [Rep.] LA (U. S.)*, 1994, **748**, 86–748.
- 48 C. L. Farrow, P. Juhas, J. W. Liu, D. Bryndin, E. S. Božin, J. Bloch, T. Proffen and S. J. L. Billinge, *J. Phys.: Condens. Matter*, 2007, **19**, 335219.
- 49 J. G. Moberly, M. T. Bernards and K. V. Waynant, *J. Cheminf.*, 2018, **10**, DOI: 10.1186/s13321-018-0259-x.
- 50 R. Sachan, E. Zarkadoula, X. Ou, C. Trautmann, Y. Zhang, M. F. Chisholm and W. J. Weber, *Sculpting nanoscale functional channels in complex oxides using energetic ions and electrons*, 2018.
- 51 R. Sachan, V. R. Cooper, B. Liu, D. S. Aidhy, B. K. Voas, M. Lang, X. Ou, C. Trautmann, Y. Zhang, M. F. Chisholm and W. J. Weber, *J. Phys. Chem. C*, 2017, **121**, 975–981.
- 52 R. Sachan, Y. Zhang, X. Ou, C. Trautmann, M. F. Chisholm and W. J. Weber, *J. Mater. Res.*, 2017, **32**, 928–935.
- 53 R. Sachan, E. Zarkadoula, M. Lang, C. Trautmann, Y. Zhang, M. F. Chisholm and W. J. Weber, *Sci. Rep.*, 2016, **6**, 2–8.
- 54 G. Sattonnay, S. Moll, L. Thomé, C. Decorse, C. Legros, P. Simon, J. Jagielski, I. Jozwik and I. Monnet, *J. Appl. Phys.*, 2010, **108**, 103512.
- 55 B. J. Wuensch and K. W. Eberman, *JOM*, 2000, **52**, 19–21.
- 56 C. L. Tracy, M. Lang, F. Zhang, S. Park, R. I. Palomares and R. C. Ewing, *Prog. Nucl. Energy*, 2018, **104**, 342–358.
- 57 W. F. Cureton, R. I. Palomares, J. Walters, C. L. Tracy, C. H. Chen, R. C. Ewing, G. Baldinozzi, J. Lian, C. Trautmann and M. Lang, *Acta Mater.*, 2018, **160**, 47–56.
- 58 W. J. Weber, *Nucl. Instrum. Methods Phys. Res., Sect. B*, 2000, **166**, 98–106.
- 59 K. Schwartz, C. Trautmann, T. Steckenreiter, O. Geiß and M. Krämer, *Phys. Rev. B: Condens. Matter Mater. Phys.*, 1998, **58**, 11232–11240.
- 60 M. P. R. Waligórska, R. N. Hamm and R. Katz, *Int. J. Radiat. Appl. Instrum., Part D*, 1986, **11**, 309–319.
- 61 G. Sattonnay, S. Moll, L. Thome, C. Decorse, C. Legros, P. Simon, J. Jagielski, I. Jozwik and I. Monnet, *J. Appl. Phys.*, 2010, **108**, 13.
- 62 S. Takaki, K. Yasuda, T. Yamamoto, S. Matsumura and N. Ishikawa, *Nucl. Instrum. Methods Phys. Res., Sect. B*, 2014, **326**, 140–144.
- 63 D. L. Drey, E. C. O’Quinn, T. Subramani, K. Lilova, G. Baldinozzi, I. M. Gussev, A. F. Fuentes, J. C. Neufeind, M. Everett, D. Sprouster, A. Navrotsky, R. C. Ewing and M. Lang, *RSC Adv.*, 2020, **10**, 34632–34650.
- 64 J. Zhang, M. Toulemonde, M. Lang, J. M. Costantini, S. Della-Negra and R. C. Ewing, *J. Mater. Res.*, 2015, **30**, 2456–2466.
- 65 J. Zhang, M. Lang, R. C. Ewing, R. Devanathan, W. J. Weber and M. Toulemonde, *J. Mater. Res.*, 2010, **25**, 1344–1351.
- 66 J. Lian, L. Wang, J. Chen, K. Sun, R. C. Ewing, J. M. Farmer and L. A. Boatner, *Acta Mater.*, 2003, **51**, 1493–1502.
- 67 S.-X. Zhang, J. Liu, H. Xie, L.-J. Xu, P.-P. Hu, J. Zeng, Z.-Z. Li, L. Liu, W.-S. Ai and P.-F. Zhai, *Chin. Phys. B*, 2019, **28**, DOI: 10.1088/1674-1056/ab43bf.
- 68 M. Lang, E. C. O’Quinn, J. Shamblin and J. Neufeind, *MRS Adv.*, 2018, 1735–1747.
- 69 J. Wang, M. Lang, R. C. Ewing and U. Becker, *J. Phys.: Condens. Matter*, 2013, **25**, DOI: 10.1088/0953-8984/25/13/135001.